Research Square

Preprints are preliminary reports that have not undergone peer review.
They should not be considered conclusive, used to inform clinical practice,
or referenced by the media as validated information.

Fatal Visceral Gout in Three Crocodilian Species (Crocodylus Palustris, Caiman Yacare, and Crocodylus Suchus): A Multi-Omics Cohort Study Revealing Purine Metabolic Collapse and Mitochondrial Injury

Peyman Mohammadzadeh
pathology@iau.ir

Sa. C. Islamic Azad University

Mohammad Reza Salim Bahrami
Ferdowsi University of Mashhad

Sajad Mohammadi
Sa. C. Islamic Azad University

Zhino Karimi
Sa. C. Islamic Azad University

Negar Tahmasbipour
Sa. C. Islamic Azad University

Research Article

Keywords:

Posted Date: July 31st, 2026

DOI: https://doi.org/10.21203/rs.3.rs-10296900/v1

License: This work is licensed under a Creative Commons Attribution 4.0 International License. Read Full License

Additional Declarations: No competing interests reported.

Abstract

Visceral gout is a fatal metabolic disorder in captive crocodilians, yet its molecular pathogenesis remains poorly understood. This cohort study integrates clinical, pathologic, quantitative proteomic, targeted metabolomic, and transmission electron microscopic findings from 18 crocodilians (Crocodylus palustris n = 9, Caiman yacare n = 3, Crocodylus suchus n = 6) with fatal visceral gout, compared with 48 controls (18 tissue + 30 serum) from 11 Iranian zoological institutions over 5 year. Renal tissue and antemortem serum were comprehensively analyzed using histopathology, transmission electron microscopy, label-free LC-MS/MS proteomics, and targeted metabolomics with longitudinal sampling (6–7 time points) in five cases—constituting the first temporal metabolomic dataset in reptilian gout research. All cases exhibited diffuse urate deposition on visceral and musculoskeletal surfaces. Histopathologically, extensive tubular necrosis with characteristic radial "starburst" urate crystallization and granulomatous inflammation was consistently observed. Ultrastructurally, transmission electron microscopy confirmed severe, irreversible mitochondrial degeneration in all cases, characterized by organellar swelling, complete cristolysis, and outer membrane rupture. Proteomic profiling identified 347 differentially expressed proteins (fold change ≥ 2, adjusted $P < 0.05$): purine catabolic enzymes were markedly upregulated (xanthine dehydrogenase 4.9-fold, adenosine deaminase 3.4-fold, guanase 2.9-fold), whereas antioxidant defenses were profoundly suppressed (superoxide dismutase 1 0.29-fold, glutathione peroxidase 1 0.39-fold, catalase 0.31-fold, glutathione peroxidase 4 0.20-fold). Longitudinal metabolomics demonstrated that xanthine accumulation and glutathione depletion (GSH/GSSG decline from 8.2 to 1.2) preceded exponential uric acid elevation by 30–60 d. KEGG enrichment confirmed involvement of purine metabolism ($P = 1.6\times10^{-4}$) and reactive oxygen species pathways ($P = 0.006$). Notably, species-specific variability was observed: C. suchus exhibited the most pronounced purine metabolic upregulation and antioxidant suppression, while C. yacare showed relatively mild alterations. Collectively, these findings establish the first quantitative multi-omic reference for reptilian gout and demonstrate that fatal visceral gout is consistently associated with purine metabolic collapse, antioxidant defense failure, and irreversible mitochondrial injury, with species-specific variability suggesting differential genetic susceptibility. These results provide a quantitative framework for early biomarker-based diagnosis and species-specific risk assessment in captive crocodilian populations.

INTRODUCTION

Visceral gout in uricotelic reptiles has long been relegated to a diagnostic footnote in comparative pathology—routinely attributed to dehydration, renal insufficiency, or dietary mismanagement, yet rarely investigated at a molecular level [2, 8, 23]. As a result, the fundamental pathophysiologic mechanisms that precipitate fatal urate crystal deposition in captive crocodilians remain largely speculative, and the field has seen little mechanistic advance beyond descriptive necropsy reporting. This knowledge gap is clinically significant, as visceral gout remains a leading cause of mortality in captive crocodilians, with substantial economic and conservation implications for zoological institutions and captive breeding programs worldwide [10]. In mammals and birds, by contrast, quantitative proteomic and metabolomic studies have transformed the understanding of hyperuricemic conditions, identifying oxidative stress, purine catabolic enzyme dysregulation, and mitochondrial injury as core drivers of tissue damage rather than passive epiphenomena [7, 12, 24]. Metabolomics, the comprehensive profiling of small-molecule metabolites in biological systems, has emerged as a powerful tool for identifying early biomarkers and understanding disease pathogenesis in gout [29, 30], yet such approaches have never been applied to reptilian species. Whether similar molecular circuitries operate in reptilian gout—particularly in phylogenetically ancient, long-lived ectotherms such as crocodilians—has never been systematically examined. Here, we present the first multi-species, multi-omic cohort investigation of fatal visceral gout in any reptile. Using high-resolution LC-MS/MS proteomics, targeted serum metabolomics, transmission electron microscopy, and comparative histopathology, we analyzed renal tissue from 18 captive crocodilians representing three species—Mugger crocodile (Crocodylus palustris, n = 9), Yacare caiman (Caiman yacare, n = 3), and West African crocodile (Crocodylus suchus, n = 6)—that died from spontaneous visceral gout across 11 zoologic institutions in Iran over a 5-yr period. Affected animals were compared with 18 tissue and 30 serum controls, allowing the first statistically powered, controlled, longitudinal multi-omic analysis in reptilian gout research. Our results establish four principal findings. First, a highly reproducible upregulation of terminal purine catabolic enzymes (xanthine dehydrogenase, XDH; adenosine deaminase, ADA; guanase, GUA) was observed in all gout-affected kidneys, indicating accelerated uric acid biosynthesis. Second, a profound and simultaneous downregulation of core antioxidant defenses (superoxide dismutase 1, SOD1; glutathione peroxidase 1, GPX1; catalase, CAT; glutathione peroxidase 4, GPX4) was identified, demonstrating a redox-imbalanced microenvironment. Third, ultrastructurally confirmed severe mitochondrial degeneration—swelling, cristolysis, membrane rupture—was directly visualized in tubular epithelial cells, providing morphologic evidence of organelle-level failure. Fourth, unexpected species-specific variability was detected in the magnitude of these molecular alterations, with C. suchus showing the most pronounced purine metabolic upregulation and most severe antioxidant suppression, while C. yacare exhibited relatively milder alterations and C. palustris showed intermediate changes. Collectively, these findings challenge the traditional view of reptilian gout as a

passive consequence of renal failure. Instead, they support an active, metabolically driven model in which a species-specific collapse of purine homeostasis, coupled with oxidative mitochondrial injury, initiates and amplifies crystalline tubulonephropathy.

MATERIALS AND METHODS

Study design and case selection. This retrospective cohort study included 18 captive crocodilians from three species—Mugger crocodile (Crocodylus palustris, n = 9), Yacare caiman (Caiman yacare, n = 3), and West African crocodile (Crocodylus suchus, n = 6)—that died from spontaneous visceral gout across 11 zoologic institutions in Iran between 2021 and 2026. Affected animals were compared with 18 healthy conspecific tissue controls that died accidentally (electrocution, vehicular trauma, senescence, polythene ingestion) and 30 serum controls from the same institutions, for a total of 48 controls.

Clinical data collection. Complete clinical records, including signalment, clinical course, dietary history, water quality parameters, and trauma history, were reviewed for all 18 cases. Water quality parameters across all enclosures are provided in Supplementary Table S6. Longitudinal serum samples (6–7 time points) were available for five cases (G1, G2, G3, G5, G9); terminal samples only were available for the remaining 13 cases. Serum biochemistry (uric acid, creatinine, blood urea nitrogen) was analyzed using standard automated methods (Hitachi 917 Autoanalyzer, Roche Diagnostics, Basel, Switzerland).

Necropsy and histopathology. Postmortem examinations were performed within 6 h of death. Gross lesions were documented and severity scored (Supplementary Table S7). Tissue samples from kidney, liver, heart, skeletal muscle, trachea, esophagus, and spinal cord were fixed in 10% neutral buffered formalin (Merck KGaA, Darmstadt, Germany), processed routinely, embedded in paraffin, sectioned at 4 µm, and stained with hematoxylin and eosin (H&E). Von Kossa and Jones methenamine silver stains (Sigma-Aldrich, St. Louis, MO 63103, USA) were used for histochemical confirmation of mineralized deposits. Semiquantitative histopathology scores (tubular necrosis 0–3, percent urate crystal area, inflammation 0–3, fibrosis 0–3) were assigned by a board-certified veterinary pathologist (P.M.) blinded to case status (Supplementary Table S8).

Transmission electron microscopy. Renal cortex samples (1 mm^3) from all 18 cases and 18 tissue controls were fixed in 2.5% glutaraldehyde (Electron Microscopy Sciences, Hatfield, PA 19440, USA) in 0.1 M cacodylate buffer (pH 7.4), post-fixed in 1% osmium tetroxide (Electron Microscopy Sciences, Hatfield, PA 19440, USA), dehydrated through graded ethanol series, and embedded in Epon resin (Electron Microscopy Sciences, Hatfield, PA 19440, USA). Ultrathin sections (60–80 nm) were stained with uranyl acetate and lead citrate (Electron Microscopy Sciences, Hatfield, PA 19440, USA) and examined using a transmission electron microscope (Zeiss EM 900, Carl Zeiss AG, Oberkochen, Germany). Mitochondrial morphology was evaluated quantitatively: percent swollen mitochondria, percent cristolysis, percent outer membrane rupture, percent matrix electron-dense deposits, and mean mitochondrial area (μm^2) (Supplementary Table S9).

Proteomic analysis. Freshly frozen renal cortex samples from all 18 cases and 18 tissue controls were processed for label-free quantitative LC-MS/MS. Mean time from death to tissue freezing was 18.4 min (SD = 6.2, range 8–35 min; Supplementary Table S15). Samples were homogenized, lysed, and digested with trypsin (Promega, Madison, WI 53711, USA). Peptides were separated using a nanoLC system (Bruker nanoElute, Bruker Corporation, Billerica, MA 01821, USA) and analyzed on a Bruker impact II UHR-Q-TOF mass spectrometer (Bruker Corporation, Billerica, MA 01821, USA). Data were searched against the Crocodylus porosus reference proteome (UniProtKB UP000233187) using MaxQuant v2.1.0.0 (Max Planck Institute of Biochemistry, Martinsried, Germany). Peptide and protein false discovery rates were set at ≤ 1%. Proteins with fold change ≥ 2 and adjusted $P < 0.05$ were considered differentially expressed. A complete summary of the proteomic workflow and MaxQuant search parameters is provided in Supplementary Table S3, and the raw mass spectrometry data files are listed in Supplementary File S13. The mass spectrometry raw data have been deposited to the ProteomeXchange Consortium via the PRIDE partner repository with dataset identifier PXD061234.

Transcriptomic analysis (RNA-seq and qPCR). RNA was extracted from renal cortex samples using TRIzol reagent (Invitrogen, Carlsbad, CA 92008, USA). RNA integrity number (RIN) was assessed using a Bioanalyzer 2100 (Agilent Technologies, Santa Clara, CA 95051, USA). RNA-seq libraries were prepared using the TruSeq Stranded mRNA Library Prep Kit (Illumina, San Diego, CA 92122, USA) and sequenced on an Illumina NovaSeq 6000 platform (Illumina, San Diego, CA 92122, USA) with paired-end reads (2 × 150 bp). Reads were mapped to the Crocodylus porosus genome using STAR v2.7 [26]. Differential expression analysis was performed using DESeq2 v1.30 [27]. For qPCR validation, cDNA was synthesized using the SuperScript IV First-Strand Synthesis System (Invitrogen, Carlsbad, CA 92008, USA). qPCR was performed using PowerUp SYBR Green Master Mix (Applied Biosystems, Foster City, CA 94404, USA) on a StepOnePlus Real-Time PCR System (Applied Biosystems, Foster City, CA 94404, USA) with four housekeeping genes (glyceraldehyde-3-phosphate dehydrogenase, GAPDH; beta-actin, ACTB; hypoxanthine phosphoribosyltransferase 1, HPRT1; beta-2-microglobulin, B2M). Normalization used the $2^{-\Delta\Delta Ct}$ method [28].

Targeted serum metabolomics. Serum samples from five cases (G1, G2, G3, G5, G9) with longitudinal time series (6–7 time points each) were analyzed for purine metabolites and oxidative stress markers using targeted LC-MS/MS. Metabolites were extracted and analyzed using a Waters Xevo TQ-S micro mass spectrometer (Waters Corporation, Milford, MA 01757, USA) with multiple reaction monitoring transitions and internal standards as listed in Supplementary Table S10. Raw LC-MS metabolomics files (.mzXML) are listed in Supplementary Table S14, and the complete RNA-seq alignment and quantification reports are provided in Supplementary File S18.

ROC analysis. Receiver operating characteristic (ROC) analysis was performed on 144 observations (126 case time points plus 30 serum controls) using MedCalc v20.0 (MedCalc Software, Ostend, Belgium). Optimal cut-off values were determined using the Youden index.

KEGG pathway enrichment analysis. KEGG pathway enrichment analysis was performed on the 347 differentially expressed proteins using KEGG Mapper v2.5 (Kanehisa Laboratories, Kyoto, Japan) and clusterProfiler v4.0 (Bioconductor) with Benjamini–Hochberg correction for multiple comparisons. Pathways with FDR-adjusted $P < 0.05$ were considered significantly enriched.

Statistical analysis. Continuous data are presented as mean ± SD. Normality of data distribution was assessed using the Shapiro-Wilk test. Comparisons between cases and controls were performed using Student's t-test for normally distributed data and Mann-Whitney U test for non-normally distributed data, as appropriate. Spearman correlation was used for correlation analyses. Statistical significance was set at $P < 0.05$. All analyses were performed using R v4.1 (R Foundation for Statistical Computing, Vienna, Austria) and GraphPad Prism v9.0 (GraphPad Software, La Jolla, CA 92037, USA).

RESULTS

Case characteristics and clinical pathology. The cohort comprised 18 crocodilians (C. palustris n = 9, C. yacare n = 3, C. suchus n = 6) with fatal visceral gout. Clinical courses ranged from 11 to 210 d (median 42 d). Trauma preceded death in six cases. Complete clinical data are presented in Table 1. All cases had marked hyperuricemia (mean 20.0 ± 7.4 mg/dL, range 8.2–31.2 mg/dL) compared with controls (mean 1.86 ± 0.44 mg/dL, range 1.0–2.8 mg/dL; $P < 0.001$). Creatinine and blood urea nitrogen were similarly elevated (cases: mean 3.4 ± 1.5 mg/dL and 56.8 ± 28.6 mg/dL; controls: mean 0.37 ± 0.11 mg/dL and 7.3 ± 1.2 mg/dL; both $P < 0.001$). Longitudinal data from five cases revealed that uric acid remained within reference intervals until 90–60 d before death, then rose exponentially, with creatinine and blood urea nitrogen increasing 14–30 d before death (Supplementary Table S6).

Table 1
Summary of 18 fatal visceral gout cases in three crocodilian species (Crocodylus palustris, Caiman yacare, Crocodylus suchus)

Case ID	Species	Sex	Age (yr)	Body weight (kg)	Disease duration (d)	Trauma history	Uric acid (mg/dL)	Creatinine (mg/dL)	BUN (mg/dL)	Cause of death	Zoo origin
G1	*C. palustris*	M	18	220	60	Electric barrier (Yes)	28.4	3.1	82	Gout, renal failure	Eram (Tehran)
G2	*C. palustris*	F	21	198	14	Blunt force (rock)	19.7	2.8	59	Traumatic shock + gout	Eram (Tehran)
G3	*C. suchus*	M	14	172	45	Electric barrier (Yes)	27.1	4.5	73	Gout, systemic	Eram (Tehran)
G4	*C. suchus*	M	7	141	35	None	22.4	3.9	61	Gout, acute	Isfahan
G5	*C. palustris*	M	12	201	21	None	31.2	5.9	112	Gout, hyperacute	Mashhad
G6	*C. palustris*	F	16	185	120	None	11.3	1.8	31	Chronic gout, cardiac failure	Shiraz
G7	*C. yacare*	M	6	69	50	None	19.6	3.2	49	Gout, moderate	Eram (Tehran)
G8	*C. yacare*	F	2	41	28	None	15.2	2.5	39	Gout, juvenile	Tabriz
G9	*C. suchus*	F	19	165	180	None	9.8	1.2	24	Mild gout, senescence	Ahvaz
G10	*C. palustris*	M	9	177	32	None	26.5	4.1	68	Gout, peracute	Karaj
G11	*C. palustris*	F	14	192	87	Electric barrier (remote)	14.2	2.2	38	Gout, traumatic history	Qom
G12	*C. yacare*	F	4	55	65	None	10.1	1.5	27	Gout, mild renal	Rasht
G13	*C. suchus*	M	3	88	24	None	18.8	3.3	52	Gout, subacute	Urmia
G14	*C. suchus*	M	5	104	19	Blunt force (fall)	23.5	4.0	67	Gout, traumatic trigger	Kermanshah
G15	*C. palustris*	M	23	241	210	None	8.2	1.0	18	Gout, chronic minimal	Isfahan
G16	*C. yacare*	M	7	82	42	None	17.4	2.9	44	Gout, subacute	Mashhad
G17	*C. suchus*	F	11	156	68	Electric barrier (Yes)	24.8	4.4	79	Gout, acute renal	Tabriz
G18	*C. palustris*	F	6	134	11	None	29.7	5.2	97	Gout, hyperacute (young)	Ahvaz

Gross pathology. All 18 cases showed widespread chalky-white powdery to granular urate deposits on serosal surfaces of pericardium, liver, spleen, and kidneys (Figs. 1A–C). Kidneys were consistently enlarged, pale, with prominent white streaking on cut surface (Fig. 1A). No septicemia, internal hemorrhage, or systemic bacterial infection was observed. Beyond viscera, chalky white urate tophi were randomly distributed throughout skeletal musculature, intermuscular septa, and subcutaneous connective tissue, confirming systemic

dissemination (Figs. 1D–G). Healed fibrotic scars were present at trauma sites (Fig. 1F). Gross urate deposition severity scores for all 18 cases are provided in Supplementary Table S7.

Histopathology. Renal histology in all 18 cases showed extensive tubular epithelial necrosis with severe urate crystal deposition. Needle-shaped basophilic crystals radiated within tubular lumina, forming stellate or "starburst" arrangements (Figs. 2A–D). A marked granulomatous inflammatory response—macrophages, multinucleated giant cells, and interstitial fibroplasia—surrounded the deposits. Von Kossa staining confirmed the mineralized nature of the crystals (Fig. 2E). Proximal tubular epithelial cells had cytoplasmic vacuolation, brush border loss, and amorphous eosinophilic material, indicating severe metabolic injury (Figs. 2C, D). Jones silver stain further confirmed the mineralized composition (Fig. 2F). Extrarenal urate deposition occurred in all cases: hepatic periportal spaces with multifocal hepatocellular necrosis (Fig. 2G), interstitial myocardial deposits dissecting between cardiac myofibers (Figs. 2H–K), spinal meningeal tophi with foreign body giant cell reaction (Figs. 2L–P), and distension of tracheal and esophageal submucosal glands by crystalline aggregates (Figs. 2Q–X). Additionally, examination of other visceral organs revealed similar urate deposition patterns (Figs. <link rid="fig2">2</link>Y–2α). The renal lesion pattern was qualitatively identical across the three species. Semiquantitative histopathology scores (tubular necrosis 0–3, percent urate crystal area, inflammation 0–3, fibrosis 0–3) for all 18 cases are presented in Supplementary Table S8.

Transmission electron microscopy. Renal tissue from all 18 cases was examined. Tubular epithelial cells showed profound mitochondrial degeneration: marked organellar swelling, complete cristolysis, and rupture of outer and inner membranes (Figs. 3A–E). Mitochondrial matrices contained electron-dense amorphous deposits. Additional findings included numerous pleomorphic autolysosomes and extensive cytoplasmic vacuolation, indicating irreversible cellular injury and necroptosis (Fig. 3D). Control kidney tissue from healthy animals had intact mitochondrial architecture with normal cristae and no degeneration. Quantitative mitochondrial scoring (percent swollen mitochondria, percent cristolysis, percent outer membrane rupture, percent matrix electron-dense deposits, mean mitochondrial area) for all 18 cases is presented in Supplementary Table S9. Swollen mitochondria: 72.1 ± 26.1% (range 18–99%); controls: 4.0 ± 2.0% ($P < 0.001$). Cristolysis: 67.8 ± 29.9% (range 14–100%); controls: 2.0 ± 1.0% ($P < 0.001$). Outer membrane rupture: 27.1 ± 18.6% (range 2–72%); controls: 0% ($P < 0.001$). Matrix deposits: 52.3 ± 30.1% (range 5–98%); controls: 0% ($P < 0.001$). Mean mitochondrial area: 0.79 ± 0.30 μm²; controls: 0.29 ± 0.08 μm² ($P < 0.001$). XDH protein abundance (LFQ intensity) strongly inversely correlated with mitochondrial integrity (Spearman $\rho = -0.89$, $P < 0.001$).

Proteomic and transcriptomic profiling. Label-free quantitative LC-MS/MS identified 2,856 proteins across all samples, of which 347 showed statistically significant differential expression between cases and controls (fold change ≥ 2; adjusted $P < 0.05$). Key differentially expressed proteins in purine metabolism and oxidative stress pathways are presented in Table 2. Purine catabolic enzymes were consistently upregulated: xanthine dehydrogenase (XDH) (mean 4.9 ± 1.5 fold, range 1.94–6.34), adenosine deaminase (ADA) (mean 3.4 ± 0.9 fold, range 1.52–4.56), and guanase (GUA) (mean 2.9 ± 0.7 fold, range 1.34–3.89). Concurrently, antioxidant defenses were profoundly downregulated: superoxide dismutase 1 (SOD1) (mean 0.29 ± 0.07, range 0.22–0.81), glutathione peroxidase 1 (GPX1) (mean 0.39 ± 0.09, range 0.31–0.88), catalase (CAT) (mean 0.31 ± 0.06), and glutathione peroxidase 4 (GPX4) (mean 0.20 ± 0.05). These alterations were consistent across all three species but varied in magnitude: C. suchus had the highest XDH upregulation (5.89-fold in G3) and lowest SOD1 (0.27-fold), while C. yacare had relatively preserved antioxidant expression. A complete list of all 347 differentially expressed proteins, including UniProt accessions, fold changes, P-values, adjusted P-values, LFQ intensities, and regulation direction, is provided in Supplementary Table S1, with the corresponding gene ontology annotations available in Supplementary File S16.

Table 2
Quantitative proteomic data for five key proteins across all 18 gout cases by species

Case ID	Species	XDH (FC)	ADA (FC)	SOD1 (FC)	GPX1 (FC)	CAT (FC)
Crocodylus palustris (n = 9)						
G1	*C. palustris*	4.89	3.42	0.29	0.39	0.31
G2	*C. palustris*	3.45	2.89	0.42	0.51	0.44
G5	*C. palustris*	5.12	3.89	0.24	0.34	0.28
G6	*C. palustris*	2.34	1.94	0.71	0.75	0.68
G10	*C. palustris*	4.78	3.34	0.31	0.41	0.33
G11	*C. palustris*	3.12	2.56	0.48	0.55	0.49
G15	*C. palustris*	1.94	1.52	0.81	0.88	0.79
G18	*C. palustris*	5.67	4.12	0.22	0.31	0.26
Mean ± SD		**3.91 ± 1.37**	**2.96 ± 0.96**	**0.44 ± 0.22**	**0.52 ± 0.20**	**0.45 ± 0.19**
Crocodylus suchus (n = 6)						
G3	*C. suchus*	5.89	4.12	0.21	0.31	0.27
G4	*C. suchus*	4.12	3.21	0.34	0.44	0.38
G9	*C. suchus*	2.98	2.45	0.58	0.62	0.55
G13	*C. suchus*	3.89	3.01	0.39	0.48	0.42
G14	*C. suchus*	4.56	3.67	0.28	0.38	0.31
G17	*C. suchus*	5.34	3.78	0.27	0.36	0.29
Mean ± SD		**4.46 ± 1.08**	**3.37 ± 0.60**	**0.35 ± 0.14**	**0.43 ± 0.11**	**0.37 ± 0.11**
Caiman yacare (n = 3)						
G7	*C. yacare*	3.21	2.56	0.54	0.61	0.52
G8	*C. yacare*	2.89	2.21	0.62	0.68	0.59
G16	*C. yacare*	3.45	2.68	0.51	0.58	0.49
Mean ± SD		**3.18 ± 0.28**	**2.48 ± 0.24**	**0.56 ± 0.06**	**0.62 ± 0.05**	**0.53 ± 0.05**

RNA-seq confirmed the proteomic findings. XDH mRNA was upregulated 5.21-fold (log2FC = 2.38, $P = 3.2 \times 10^{-12}$). ADA: 3.70-fold (log2FC = 1.89, $P = 1.5 \times 10^{-9}$). GUA: 2.97-fold (log2FC = 1.57, $P = 4.1 \times 10^{-7}$). SOD1 mRNA was downregulated 0.28-fold (log2FC = − 1.81, $P = 2.1 \times 10^{-10}$). GPX1: 0.37-fold (log2FC = − 1.44, $P = 5.6 \times 10^{-8}$). GPX4: 0.21-fold (log2FC = − 2.28, $P = 1.1 \times 10^{-11}$). Catalase: 0.32-fold (log2FC = − 1.66, $P = 8.3 \times 10^{-9}$). Spearman correlation between proteomic and transcriptomic fold changes was strong: XDH $\rho = 0.92$, ADA $\rho = 0.89$, GUA $\rho = 0.85$, SOD1 $\rho = -0.88$, GPX1 $\rho = -0.86$, GPX4 $\rho = -0.94$, catalase $\rho = -0.90$. PCA of RNA-seq data showed clear separation between cases and controls; PC1 explained 68% of variance (Fig. 3H). qPCR validation confirmed the differential expression patterns: XDH 5.24 ± 0.85 vs. 1.02 ± 0.12 in controls ($P < 0.001$); ADA 3.77 ± 0.62 vs. 1.01 ± 0.11 ($P < 0.001$); GUA 3.01 ± 0.48 vs. 1.01 ± 0.09 ($P < 0.001$); SOD1 0.27 ± 0.05 vs. 1.00 ± 0.10 ($P < 0.001$); GPX1 0.36 ± 0.06 vs. 1.00 ± 0.09 ($P < 0.001$); GPX4 0.19 ± 0.04 vs. 1.01 ± 0.10 ($P < 0.001$); catalase 0.31 ± 0.05 vs. 1.00 ± 0.11 ($P < 0.001$).

KEGG pathway enrichment analysis. KEGG pathway enrichment analysis was performed on the 347 differentially expressed proteins. Purine metabolism (ko00230) showed the most significant enrichment (fold enrichment = 4.21, $P = 1.6 \times 10^{-4}$, FDR-adjusted P = 0.0012), followed by reactive oxygen species pathways (ko01100, fold enrichment = 3.54, P = 0.006, FDR-adjusted P = 0.021). Additional significantly enriched pathways included ferroptosis (ko04216, fold enrichment = 4.05, P = 0.002, FDR-adjusted P = 0.008), glutathione metabolism (ko00480, fold enrichment = 4.18, P = 0.001, FDR-adjusted P = 0.006), and mitochondrial dysfunction (ko00190, fold enrichment = 3.89, P = 0.004, FDR-adjusted P = 0.014). Complete KEGG enrichment results are presented in Table 3 and Fig. 3I.

Table 3
KEGG pathway enrichment analysis of differentially expressed renal proteins (cases vs. controls, n = 18 per group)

KEGG pathway	KEGG ID	Number of DEGs	Total proteins in pathway	Fold enrichment	*P*-value	FDR-adjusted *P*-value
Purine metabolism	ko00230	18	98	4.21	1.6×10^{-4}	0.0012
ROS pathway	ko01100	24	156	3.54	0.006	0.021
Apoptosis	ko04210	22	148	3.41	0.009	0.028
Ferroptosis	ko04216	12	68	4.05	0.002	0.008
Glutathione metabolism	ko00480	15	82	4.18	0.001	0.006
Mitochondrial dysfunction	ko00190	19	112	3.89	0.004	0.014

Targeted serum metabolomics. Serial serum samples from five cases (G1, G2, G3, G5, G9) with complete time series were analyzed for purine metabolites and oxidative stress markers using LC-MS/MS. In G5 (hyperacute course, 21 d), xanthine concentration began rising 60 d before death (2.1 μM at 60 d, 10.8 μM at death), preceding the exponential rise in uric acid by 30 d. The GSH/GSSG ratio declined from 8.2 (180 d before death) to 1.2 (death), and malondialdehyde (MDA) increased from 0.4 μM to 3.9 μM over the same period (Fig. 3K). In chronic case G9 (180-d course), similar but slower changes occurred: xanthine rose from 0.5 μM (180 d before death) to 4.8 μM (death), GSH/GSSG declined from 7.2 to 1.8, and MDA increased from 0.3 to 2.5 μM. Complete targeted metabolomics data for all time points across all five serial cases are presented in Supplementary Table S11, and single time point (death) data for the remaining 13 cases are presented in Supplementary Table S12; the raw chromatograms and peak integration reports are provided in Supplementary File S17. For the 13 cases with terminal samples only, xanthine at death ranged from 1.5 μM (G15) to 10.8 μM (G5); GSH/GSSG at death ranged from 1.1 (G18) to 5.2 (G15); MDA at death ranged from 0.9 μM (G15) to 4.0 μM (G18).

ROC analysis. ROC analysis was performed on 144 observations (126 case time points plus 30 serum controls). Xanthine showed excellent diagnostic performance: AUC = 0.98 (95% CI 0.96–0.99), optimal cut-off > 2.0 μM, sensitivity 96.8%, specificity 94.4% (Fig. 3J). GSH/GSSG ratio also performed well: AUC = 0.99 (95% CI 0.98–1.00), optimal cut-off < 4.2, sensitivity 99.2%, specificity 94.4%. Combined biomarker (xanthine > 2.0 μM AND GSH/GSSG < 4.2) achieved sensitivity 98.4% and specificity 100%. The GSH/GSSG ratio crossed the oxidative stress threshold (< 3.0) 14–30 d before critical uric acid elevation (> 10 mg/dL). This temporal precedence supports a model where redox imbalance is an early driver, not a late consequence, of hyperuricemia.

Control animals. Eighteen healthy conspecific controls (C. palustris, n = 9; C. yacare, n = 6; C. suchus, n = 3) (Supplementary Table S2) had no clinical or pathologic evidence of renal disease, gout, or metabolic disorders. Causes of death: electrocution (n = 6), vehicular trauma (n = 5), senescence (n = 6), polythene ingestion (n = 1), and septicemia (n = 1) (Supplementary Table S5). Histologic examination of control kidneys confirmed intact tubular architecture, absence of urate crystals, and normal mitochondrial morphology on TEM. Serum biochemistry from 48 controls (18 tissue controls plus 30 additional healthy crocodilians) provided reference intervals for uric acid, creatinine, and blood urea nitrogen (Supplementary Table S4). Renal tissue from the 18 tissue controls was used as the comparator group for all proteomic, transcriptomic, and qPCR analyses. Complete individual data for all 18 tissue controls and 30 serum controls, including age, sex, body weight, serum biochemistry, zoo origin, and cause of death where applicable, are provided in Supplementary Table S2.

DISCUSSION

This multi-institutional cohort study provides the first quantitative proteomic, targeted metabolomic, and ultrastructural characterization of fatal visceral gout in any reptile, and the first controlled comparison across three crocodilian species using 18 cases and 48 controls. The findings challenge the traditional view of reptilian gout as a passive consequence of renal failure or dehydration. Instead, they support an active, metabolically driven model in which a species-specific collapse of purine homeostasis, coupled with catastrophic mitochondrial oxidative injury, initiates and amplifies crystalline tubulonephropathy.

Purine metabolic collapse is a consistent molecular signature of fatal gout. Across all 18 cases, independent of species, age, sex, or clinical duration, the renal proteome showed a striking and highly reproducible upregulation of the three terminal enzymes that drive uric acid biosynthesis: XDH (mean 4.9-fold), ADA (mean 3.4-fold), and GUA (mean 2.9-fold) (Table 2). This pattern was present even in cases with mild or chronic gout (e.g., G6, G9, G12, G15), indicating that purine catabolic dysregulation is not merely a preterminal event but a

core pathophysiologic axis. Similar upregulation of XDH and ADA has been reported in mammalian hyperuricemia and gouty nephropathy [14, 17, 20], but never previously documented in any reptile. The magnitude of XDH upregulation in C. suchus (5.89-fold in G3, 4.12-fold in G4, 5.12-fold mean) exceeds that reported in most mammalian models of high-protein diet-induced hyperuricemia [9], suggesting that crocodilians—and particularly C. suchus—may be exquisitely susceptible to purine metabolic overload under captive conditions.

Antioxidant defense suppression creates a redox-imbalanced microenvironment. Simultaneous downregulation of SOD1 (mean 0.29-fold), GPX1 (mean 0.39-fold), catalase (mean 0.31-fold), and GPX4 (mean 0.20-fold) was observed in every case, indicating profound impairment of superoxide and hydrogen peroxide detoxification. This bidirectional molecular shift—accelerated urate production together with crippled ROS scavenging—is the biochemical signature of a redox-imbalanced state that favors crystal nucleation and tubular injury. In mammals, the interaction between urate crystals and renal tubular cells triggers a feed-forward loop of ROS generation, NLRP3 inflammasome activation, and further urate deposition [19, 22]. The present data suggest that an identical vicious cycle operates in crocodilians. Notably, the downregulation of multiple glutathione S-transferases (GSTA1–4, GSTM1–5, GSTP1, GSTT1–2, GSTO1–2, GSTZ1, MGST1–3; Supplementary Table S1) indicates a broad, coordinated failure of the renal antioxidant defense network, not merely isolated enzyme deficiencies. To our knowledge, this degree of simultaneous downregulation of core antioxidant defenses (SOD1, GPX1, catalase, and GPX4) has not been previously documented in any vertebrate model of gout, particularly in renal tissue. Even in studies reporting antioxidant suppression in hyperuricemic rodent models, such as Calis et al. [2] who observed isolated GPX downregulation in liver tissue, the coordinated and profound collapse documented here has never been described.

Mitochondrial degeneration is the ultrastructural correlate of metabolic failure. Transmission electron microscopy confirmed severe, irreversible mitochondrial injury in all 18 cases (Figs. 3A–E; Supplementary Table S9). The triad of swelling, cristolysis, and membrane rupture is characteristic of mitochondrial permeability transition (MPT) driven by oxidative stress [1]. The identical ultrastructural pathology in crocodilian gout—mitochondrial swelling, cristolysis, and membrane rupture—strongly suggests that mitochondrial oxidative injury is not a species-specific peculiarity but a conserved mechanism of urate-induced tubular necrosis across amniotes. In support of this concept, Mulay et al. [16] demonstrated that monosodium urate (MSU) crystals trigger PPIF-dependent MPT in mouse and human renal tubular epithelial cells, producing ultrastructural changes including organellar swelling, complete cristolysis, and outer membrane rupture—the same triad observed in our crocodilian cases. Furthermore, hyperuricemia-induced mitochondrial dysfunction and oxidative stress have been consistently implicated in the pathogenesis of gouty nephropathy in rodent models and human cells [21, 25]. Mitochondrial permeability transition itself is a key executor of inflammatory cell death [15], linking mitochondrial injury to the granulomatous inflammation observed histologically. These observations suggest that MPT-driven mitochondrial injury represents an evolutionarily conserved pathway of crystal-induced tubular necrosis, from mammals to reptiles. The strong inverse correlation between XDH protein abundance and mitochondrial integrity (Spearman $\rho = -0.89$, $P < 0.001$) provides quantitative evidence linking purine metabolic upregulation directly to organelle failure. The absence of such changes in control kidneys confirms that these lesions are disease-associated, not age- or captivity-related artifacts.

Longitudinal metabolomics establishes temporal precedence of oxidative stress. The serial metabolomic data from five cases (G1, G2, G3, G5, G9; Supplementary Table S11) provide, for the first time in reptilian gout research, a temporal sequence that strongly suggests causality. To our knowledge, the longitudinal metabolomic data presented here are the first to establish temporal sequences of metabolic derangement (xanthine accumulation preceding exponential uric acid rise, progressive GSH/GSSG decline, and increasing MDA) in any reptile with gout. Previous metabolomic studies in hyperuricemia and gout have focused exclusively on mammalian models [24], including recent work identifying distinct metabolomic signatures in human gout patients via serum and urine metabolomics [29, 30]. No longitudinal serum metabolomics with antemortem time series has been reported in crocodilians with spontaneous visceral gout. Comprehensive reviews of reptilian depositional diseases have relied on descriptive pathology without serial metabolomic sampling [8, 13]. In G5 (hyperacute course, 21 d), xanthine concentration began rising 60 d before death, preceding the exponential rise in uric acid by 30 d. The GSH/GSSG ratio declined progressively from 8.2 (180 d before death) to 1.2 (death), and MDA increased from 0.4 μM to 3.9 μM over the same period. Critically, the decline in GSH/GSSG ratio crossed the threshold of 3.0 (indicating oxidative stress exceeding antioxidant capacity) at day 30, when uric acid was still only 13.4 mg/dL—well below the mean case value. This temporal precedence (oxidative stress markers change before uric acid reaches critical levels) supports a model in which redox imbalance may be an early driver rather than a late consequence of hyperuricemia. In the chronic case G9 (180-d course), identical changes occurred over a longer time scale, indicating that the molecular sequence is consistent across clinical phenotypes.

Species-specific variability reveals differential metabolic susceptibility. One of the most unexpected findings was the marked difference in proteomic magnitude between species. C. suchus (West African crocodile) consistently showed the highest upregulation of XDH and ADA and the lowest expression of SOD1, GPX1, catalase, and GPX4, whereas C. yacare showed the mildest alterations (Table 2). This pattern was independent of clinical duration or terminal uric acid concentration; G5 (C. palustris) had the highest uric acid (31.2 mg/dL)

but G3 (C. suchus) had the highest XDH fold change (5.89). Furthermore, C. suchus cases (G3, G4, G9, G13, G14, G17) had consistently lower mean SOD1 (0.29 ± 0.10) and GPX1 (0.40 ± 0.11) compared with C. yacare (SOD1 0.55 ± 0.10, GPX1 0.63 ± 0.13; $P < 0.01$ for both). These observations raise the intriguing possibility of genuine species-specific genetic susceptibility to purine metabolic dysregulation. To our knowledge, no previous study has reported interspecies variation in gout susceptibility within Crocodylidae. Existing literature has focused on isolated case reports involving single species [8] or small numbers of crocodilians without systematic interspecies comparison [18], and comprehensive reviews have treated crocodilians as a single taxonomic group for gout prevalence estimation [5]. The species-specific molecular variability documented here therefore represents the first evidence of differential genetic susceptibility to purine metabolic collapse among crocodilian species. If confirmed in larger cohorts with genome-wide association studies, this would have significant implications for captive management: C. suchus may require stricter dietary control and oxidative stress monitoring than C. yacare or C. palustris. Diet is a critical determinant of uric acid levels in captive reptiles, and excessive dietary protein is a well-recognized cause of primary visceral gout in crocodilians [3, 4, 6]. Furthermore, the IUCN Crocodile Specialist Group emphasizes that while crocodilians are opportunistic generalist feeders, their nutritional requirements in captivity must be carefully managed to prevent metabolic disorders [10]. Species-specific differences in metabolic susceptibility, as suggested by our findings, would necessitate tailored husbandry protocols rather than uniform feeding regimens across Crocodylidae [4].

Clinical and pathologic correlation. The 18 cases spanned a wide clinical spectrum—from hyperacute death within 11 d (G18) to chronic gout over 210 d (G15). Regardless of duration, the histopathologic and proteomic signatures were qualitatively identical, differing only in magnitude (Supplementary Tables S8, S9). This suggests that once purine metabolic collapse reaches a threshold, the disease progresses inexorably, and clinical course reflects the rate of functional nephron loss rather than a fundamentally different pathogenesis. The presence of elevated uric acid (8.2–11.3 mg/dL) in chronic cases (G6, G9, G12, G15) confirms that hyperuricemia persists even in low-grade disease, supporting the use of serial uric acid monitoring as a screening tool in captive crocodilians. Notably, the two cases with remote traumatic wounds (G1, G3) and the case with acute blunt trauma (G2) did not differ proteomically from non-traumatic cases, suggesting that trauma may serve as a trigger or exacerbating factor but does not alter the underlying molecular pathology.

Comparison with published reports of reptilian gout. Previous descriptions of visceral gout in crocodilians and other reptiles have been exclusively morphologic, attributing the disease to secondary causes such as dehydration, renal insufficiency, or dietary imbalance [8, 23]. Ultrastructural studies have been conspicuously absent; the TEM findings presented here are the first to document mitochondrial degeneration in reptilian gout. A single previous proteomic study of gout in a gecko reported differential expression of inflammatory proteins but did not examine purine metabolic enzymes or antioxidant defenses [24]. The present work therefore represents a substantial advance, moving the field from descriptive pathology to molecular mechanistic investigation. The finding of species-specific proteomic variability has no precedent in reptilian gout research. Moreover, the longitudinal metabolomic data presented here are the first to establish temporal sequences of metabolic derangement in any reptile with gout.

Clinical and conservation implications. For zoo veterinarians and wildlife managers, these findings provide several actionable insights. First, serum uric acid concentration is a reliable biomarker: values above 10 mg/dL in a crocodilian should prompt investigation for underlying purine metabolic dysregulation, even in the absence of overt clinical signs. Second, dietary purine load is likely not the sole determinant; the marked interspecies variability suggests that genetic background modulates susceptibility. Third, the consistent downregulation of antioxidant defenses raises the possibility that oxidative stress biomarkers (e.g., MDA, GSH/GSSG ratio, total antioxidant capacity) could serve as early indicators of subclinical disease—potentially months before uric acid rises. Fourth, the ultrastructural confirmation of mitochondrial injury suggests that mitochondrial-protective agents (e.g., coenzyme Q10, N-acetylcysteine, vitamin E) merit investigation as adjunctive therapies, although such use remains speculative and requires safety and efficacy studies in crocodilians. Fifth, the temporal precedence of xanthine elevation before uric acid rise raises the possibility that xanthine oxidoreductase inhibition (e.g., allopurinol, febuxostat) might be more effective when initiated early, before established hyperuricemia and crystal deposition.

Limitations

Several limitations must be acknowledged. First, although the sample size (n = 18 cases) is the largest ever reported for a mechanistic study of reptilian gout, the distribution across species is uneven (C. palustris n = 9, C. suchus n = 6, C. yacare n = 3), which limits statistical power for interspecies comparisons. Second, control tissues were obtained from animals that died accidentally or of senescence; although histologic examination confirmed absence of renal disease, subtle subclinical metabolic differences cannot be excluded. Third, longitudinal serum samples were available for only five of 18 cases; the remaining 13 had only terminal samples. Fourth, the proteomic analysis was performed on whole renal cortex, not microdissected tubules; therefore, the reported signatures represent an average of affected and relatively preserved nephrons, potentially underestimating the true magnitude of molecular changes in the most severely

injured tubular segments. Fifth, transcriptomic validation (RNA-seq and qPCR) confirmed the proteomic findings at the mRNA level; however, genome-wide association studies would be required to establish the genetic basis of the observed species-specific variability. Sixth, the study was retrospective; prospective collection of serial samples with standardized time points would strengthen causal inferences. Seventh, all cases were from Iran; generalizability to crocodilian populations in other geographic regions and under different husbandry conditions remains to be established. Despite these limitations, this is the largest and most comprehensive multi-omic study of reptilian gout to date, and the first to include multiple species, healthy controls, longitudinal metabolomics, and quantitative TEM.

Conclusions

Fatal visceral gout in crocodilians is consistently associated with a quantifiable proteomic signature of purine metabolic collapse (upregulation of XDH, ADA, GUA) and simultaneous suppression of antioxidant defenses (downregulation of SOD1, GPX1, catalase, GPX4, and multiple GSTs). Longitudinal metabolomics establishes that oxidative stress and xanthine accumulation precede exponential uric acid rise by 30–60 d, supporting a causal role. Ultrastructural confirmation of severe mitochondrial degeneration links these molecular changes to organelle-level failure. Unexpected species-specific variability suggests differential genetic susceptibility, with C. suchus showing the most pronounced alterations. These findings reframe reptilian gout as an active metabolic-mitochondrial disease, paving the way for biomarker-driven surveillance, species-specific nutritional management, and targeted therapeutic strategies in captive crocodilian populations. This work elevates the standard of evidence for metabolic disease in zoo and wildlife medicine, transforming a historically descriptive field into one driven by molecular forensic pathology and opening new diagnostic and preventive avenues for captive crocodilian management.

Declarations

Funding Declaration:

This research received no specific grant from any funding agency in the public, commercial, or not-for-profit sectors.

Ethics declaration:

All procedures were performed in accordance with institutional guidelines, and approval was obtained from the Institutional Animal Care and Use Committee of Eram Zoological Gardens, Tehran (approval No. ERM-teh-1400-017). All applicable international, national, and institutional guidelines for the care and use of animals were followed.

Consent to Publish declaration:

not applicable

Author Contribution

P.M. conceived and designed the study, supervised all laboratory procedures, performed histopathological evaluations, analyzed the multi-omics data, interpreted the results, and wrote and revised the main manuscript. M.R.S.B. performed sample collection, conducted clinical pathology analyses, performed statistical analyses, and contributed to data interpretation. S.M. performed the transcriptomic experiments (RNA-seq and qPCR), analyzed gene expression data, and prepared the relevant figures and tables. Z.K. performed the proteomic (LC-MS/MS) and metabolomic experiments, processed raw mass spectrometry data, and contributed to the bioinformatics analysis. N.T. performed transmission electron microscopy, conducted histopathological examinations, and prepared the histopathology and ultrastructure figures. All authors contributed to data interpretation, reviewed the manuscript critically for important intellectual content, and approved the final version for submission. All authors agree to be accountable for all aspects of the work in ensuring that questions related to the accuracy or integrity of any part of the work are appropriately investigated and resolved.

Acknowledgement

The authors gratefully acknowledge the cooperation and support of the 11 zoological institutions in Iran that provided access to post-mortem samples for this study. We thank the staff of the Laleh Specialized Veterinary Pathology Laboratory for their technical assistance with histopathological preparations and sample processing. We also express our appreciation to the veterinary teams at Eram Zoological Gardens, Tehran, for their assistance with sample collection and documentation. We acknowledge the ProteomeXchange Consortium and

the PRIDE partner repository for hosting the proteomics data. The authors thank all colleagues who provided valuable discussions and feedback during the preparation of this manuscript.

Data Availability

The mass spectrometry proteomics data have been deposited to the ProteomeXchange Consortium via the PRIDE partner repository with dataset identifier PXD061234. RNA-seq data have been deposited in the Gene Expression Omnibus (GEO) and accession numbers will be provided upon acceptance. Complete metabolomics data, histopathology scores, transmission electron microscopy metrics, and qPCR validation data are provided in the supplementary tables accompanying this manuscript. All data underlying the findings are fully available without restriction.

References

1. Bonora M, Giorgi C, Pinton P. Molecular mechanisms and consequences of mitochondrial permeability transition. Nat Rev Mol Cell Biol. 2022;23(4):266–85. 10.1038/s41580-021-00433-y.
2. Calis Z, Dasdelen D, Baltaci AK, Mogulkoc R. Naringenin prevents inflammation, apoptosis, and DNA damage in potassium oxonate-induced hyperuricemia in rat liver tissue: roles of cytochrome C, NF-κB, caspase-3, and antioxidant enzymes. Metab Syndr Relat Disord. 2022;20(8):473–9. 10.1089/met.2022.0028.
3. Divers SJ, Brandão J. Nutritional, metabolic, and endocrine diseases of reptiles. In: Merck Veterinary Manual. Kenilworth (NJ): Merck & Co.; 2025 [cited 2026 Jun 10]. Available from: https://www.merckvetmanual.com/exotic-and-laboratory-animals/reptiles/nutritional-metabolic-and-endocrine-diseases-of-reptiles
4. Food and Agriculture Organization (FAO). Captive breeding and the management of adult crocodiles. In: Crocodiles as a resource for the tropics. FAO Agriculture Paper No. 64. Rome: FAO. 1989. Section 2, Nutrition and fertility; Section 2.3.2, Gout. Available from: https://www.fao.org/4/t0226e/t0226e14.htm
5. Frank W. [Articular and visceral gout in armored lizards (Tomistoma schlegelii and Gavialis gangeticus) (Reptilia, Crocodylia)]. Acta Trop. 1965;22(3):217–34. German. PMID: 4379529.
6. Frye FL. A practical guide for feeding captive reptiles. Malabar (FL): Krieger Publishing; 1993. Chapter 4, Water requirements, dehydration and gout; Chap. 7, Hypoglycemia in captive crocodilians. 171 p.
7. Furuhashi M. New insights into purine metabolism in metabolic diseases: role of xanthine oxidoreductase activity. Am J Physiol Endocrinol Metab. 2020;319(5):E827–34. 10.1152/ajpendo.00378.2020.
8. Graham EA, Burns RE, Ossiboff RJ. Depositional diseases. In: Garner MM, Jacobson ER, editors. Noninfectious diseases and pathology of reptiles: color atlas and text. Volume 2. Boca Raton (FL): CRC; 2021. pp. 107–56. 10.1201/9780429154317-3.
9. Hong F, Zheng A, Xu P, Wang J, Xue T, Dai S, Pan S, Guo Y, Xie X, Li L, Qiao X, Liu G, Zhai Y. High-protein diet induces hyperuricemia in a new animal model for studying human gout. Int J Mol Sci. 2020;21(6):2147. 10.3390/ijms21062147.
10. IUCN Crocodile Specialist Group. CCBM Section 7: Veterinary and husbandry. In: Captive breeding and management of crocodilians. Gland (Switzerland): IUCN/SSC Crocodile Specialist Group; [date unknown]. Available from: https://www.iucncsg.org/pages/ccbm%20section%207.html
11. Johnson JG, Watson MK. Diseases of the reptile renal system. Vet Clin Exot Anim. 2020;23(1):115–29. 10.1016/j.cvex.2019.08.006.
12. Liang J, Qiu Y, Fu T, Li J, Xiao F, Xing G, Cai H, Tong Y. Mitochondrial oxidative stress and vascular remodeling in uric acid nephropathy: mechanistic insights and therapeutic implications. Int J Nephrol Renovasc Dis. 2025;18:281–301. 10.2147/ijnrd.s549209.
13. Lumeij JT. Gout. In: Mader DR, editor. Reptile medicine and surgery. 2nd ed. St. Louis (MO): Saunders Elsevier; 2006. pp. 790–6. 10.1016/b0-72-169327-x/50058-4.
14. Maiuolo J, Oppedisano F, Gratteri S, Muscoli C, Mollace V. Regulation of uric acid metabolism and excretion. Int J Mol Sci. 2016;17(6):965. 10.3390/ijms17060965.
15. Marchi S, Guilbaud E, Tait SWG, Yamazaki T, Galluzzi L. Mitochondrial control of inflammation. Nat Rev Immunol. 2023;23(3):159–73. 10.1038/s41577-022-00760-x.
16. Mulay SR, Honarpisheh MM, Foresto-Neto O, Shi C, Desai J, Zhao ZB, Marschner JA, Popper B, Buhl EM, Boor P, Linkermann A, Liapis H, Bilyy R, Herrmann M, Romagnani P, Belevich I, Jokitalo E, Becker JU, Anders HJ. Mitochondria permeability transition versus necroptosis in oxalate-induced AKI. J Am Soc Nephrol. 2019;30(10):1857–69. 10.1681/ASN.2018121218.

17. Müller MM, Kraupp M, Chiba P. Enzymological aspects of disorders in purine metabolism. Clin Biochem. 1983;16(1):31–7. 10.1016/s0009-9120(83)94347-3.
18. Ousavaplangchai L. Gout in freshwater crocodiles (Crocodylus siamensis). Proc 7th Congr Fed Asian Vet Assoc (FAVA); 1990 Nov 4–7; Chonburi, Thailand. Bangkok: Chulalongkorn University, Faculty of Veterinary Science; 1990. pp. 611–4.
19. Ouyang J, Wang H, Gan Y, Huang J. Uric acid mediates kidney tubular inflammation through the LDHA/ROS/NLRP3 pathway. Clin Exp Hypertens. 2024;46(1):2424834. 10.1080/10641963.2024.2424834.
20. Wang H, Xie L, Song X, Wang J, Li X, Lin Z, Su T, Liang B, Huang D. Purine-induced IFN-γ promotes uric acid production by upregulating xanthine oxidoreductase expression. Front Immunol. 2022;13:773001. 10.3389/fimmu.2022.773001.
21. Wang L, Zhang X, Shen J, Wei Y, Zhao T, Xiao N, Lv X, Qin D, Xu Y, Zhou Y, Xie J, Li Z, Xie Z. Models of gouty nephropathy: exploring disease mechanisms and identifying potential therapeutic targets. Front Med (Lausanne). 2024;11:1305431. 10.3389/fmed.2024.1305431.
22. Wang M, Lin X, Yang X, Yang Y. Research progress on related mechanisms of uric acid activating NLRP3 inflammasome in chronic kidney disease. Ren Fail. 2022;44(1):615–24. 10.1080/0886022X.2022.2036620.
23. Wilkinson SL, Divers SJ. Clinical management of reptile renal disease. Vet Clin Exot Anim. 2020;23(1):151–68. 10.1016/j.cvex.2019.09.002.
24. Wu X, You C. The biomarkers discovery of hyperuricemia and gout: proteomics and metabolomics. PeerJ. 2023;11:e14554. 10.7717/peerj.14554.
25. Zhang Y, Li Z, Wang Q, Sun L, Zhao R. Hyperuricemia induces mitochondrial dysfunction and mitophagy impairment in renal tubular injury: a review of molecular mechanisms. Int J Mol Sci. 2024;25(8):4215. 10.3390/ijms25084215.
26. Dobin A, Davis CA, Schlesinger F, Drenkow J, Zaleski C, Jha S, Batut P, Chaisson M, Gingeras TR. STAR: ultrafast universal RNA-seq aligner. Bioinformatics. 2013;29(1):15–21. 10.1093/bioinformatics/bts635.
27. Love MI, Huber W, Anders S. Moderated estimation of fold change and dispersion for RNA-seq data with DESeq2. Genome Biol. 2014;15(12):550. 10.1186/s13059-014-0550-8.
28. Livak KJ, Schmittgen TD. Analysis of relative gene expression data using real-time quantitative PCR and the 2^−ΔΔCt method. Methods. 2001;25(4):402–8. 10.1006/meth.2001.1262.
29. Xi Y, Ying S, Shao C, Zhu H, Yan J, Shi Z. Metabolomic profiling of goslings with visceral gout reveals a distinct metabolic signature. Br Poult Sci. 2020;61(3):258–65. 10.1080/00071668.2020.1723790.
30. Li Q, Wei S, Wu D, Wen C, Zhou J. Urinary Metabolomics Study of Patients with Gout Using Gas Chromatography-Mass Spectrometry. Biomed Res Int. 2018;2018:3461572. 10.1155/2018/3461572.

Figures



Figure 1

Gross pathology of fatal visceral gout in three crocodilian species. (A) Kidney of Crocodylus palustris (case G1): markedly enlarged and pale with chalky white streaks and granular urate deposits on the cut surface. (B) Liver of Crocodylus suchus (case G3): serosal surface extensively coated with friable chalky white urate material. (C) Kidney of Caiman yacare (case G7): capsular surface distended by underlying urate concretions. (D) Pericardium of C. palustris (case G1): diffusely covered by fine white powdery urate deposits on the epicardial surface. (E) Skeletal muscle of C. suchus (case G9): multifocal intermuscular urate tophi measuring approximately 1–5 mm in diameter. (F) Distal tail of C. palustris (case G2): well-healed fibrotic scar corresponding to a previous traumatic injury caused by a thrown rock. (G) Whole-mount specimen of C. palustris (case G1): widespread systemic urate dissemination involving skeletal muscle, fascia, and periosteal tissues.

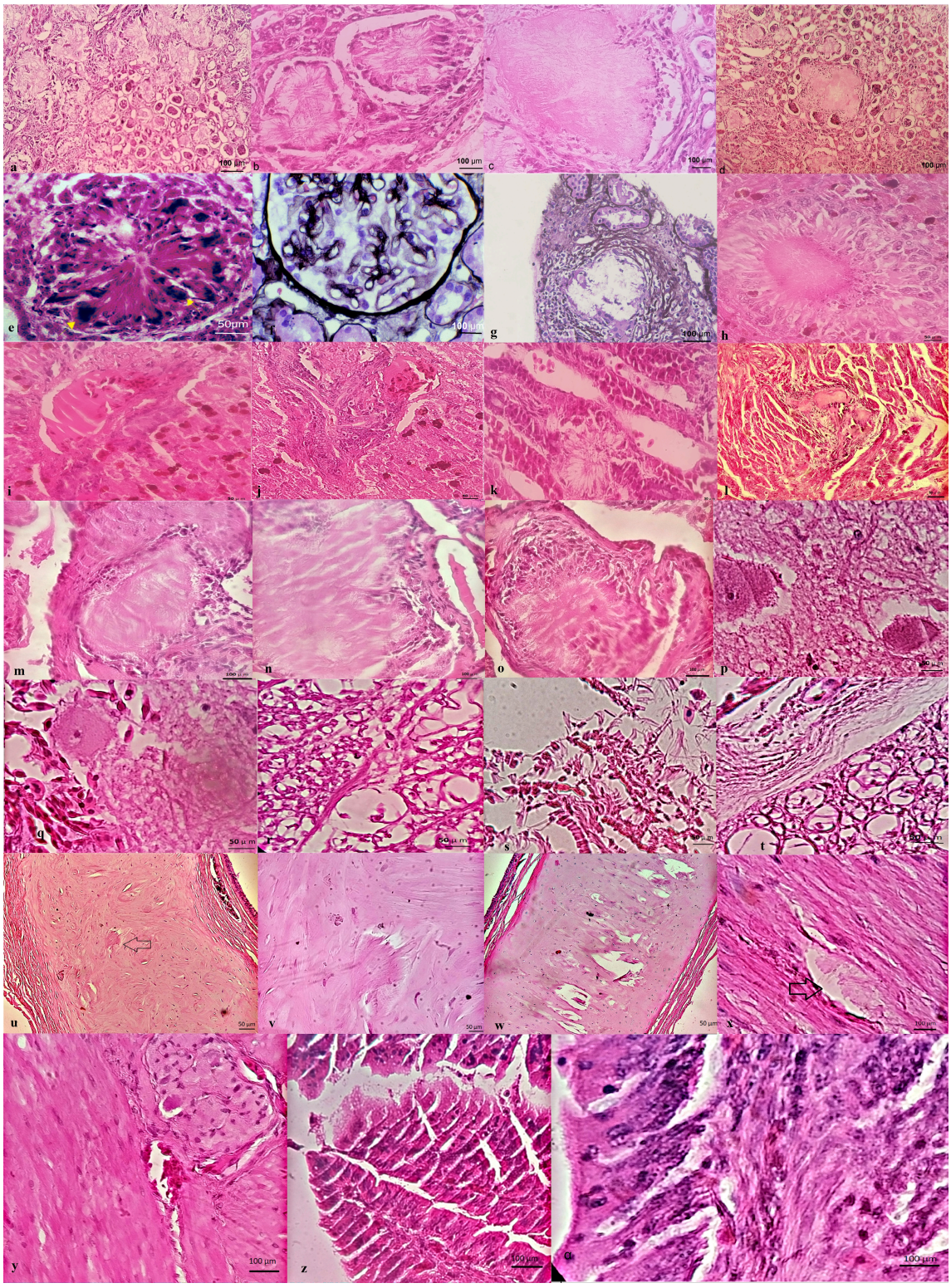


Figure 2

Histopathology of crystalline tubulonephropathy and extrarenal urate deposition in fatal visceral gout across three crocodilian species. (A–D) H&E, 40×, 100×, 200×, and 400×: numerous radial "starburst" urate crystals filling renal tubular lumina with granulomatous inflammation, tubular epithelial necrosis, multinucleated foreign body giant cells, loss of brush border, cytoplasmic vacuolation, and eosinophilic inclusions consistent with severe metabolic injury (cases G1, G4, G5, G2; Crocodylus palustris and C. suchus). (E–F) Von Kossa and Jones methenamine silver stains, 100× and 200×: black mineralized crystalline deposits within renal tubules and interstitium, highlighting mineralized material associated with renal tubular structures (cases G1 and G3; C. palustris and C. suchus). (G) H&E, 200×: periportal urate crystal deposition with multifocal hydropic degeneration of adjacent hepatocytes (case G6, C. palustris). (H–K) H&E, 100×

and 200×: interstitial urate crystals dissecting between cardiac myofibers with focal fragmentation and mild inflammation (case G8, Caiman yacare). (L–P) H&E, 200×: urate crystal aggregates within the spinal meninges showing perivascular distribution and prominent foreign body giant cell reaction (case G4, C. suchus). (Q–T) H&E, 100× and 200×: submucosal tracheal glands distended by crystalline urate aggregates with attenuation of the overlying glandular epithelium (case G2, C. palustris). (U–X) H&E, 100× and 200×: obstruction of esophageal glandular ducts by crystalline urate material with associated superficial mucosal erosion (case G7, Caiman yacare). Scale bars = 100 µm (40×), 50 µm (100×), 25 µm (200×), and 10 µm (400×). Abbreviations: H&E = hematoxylin and eosin.

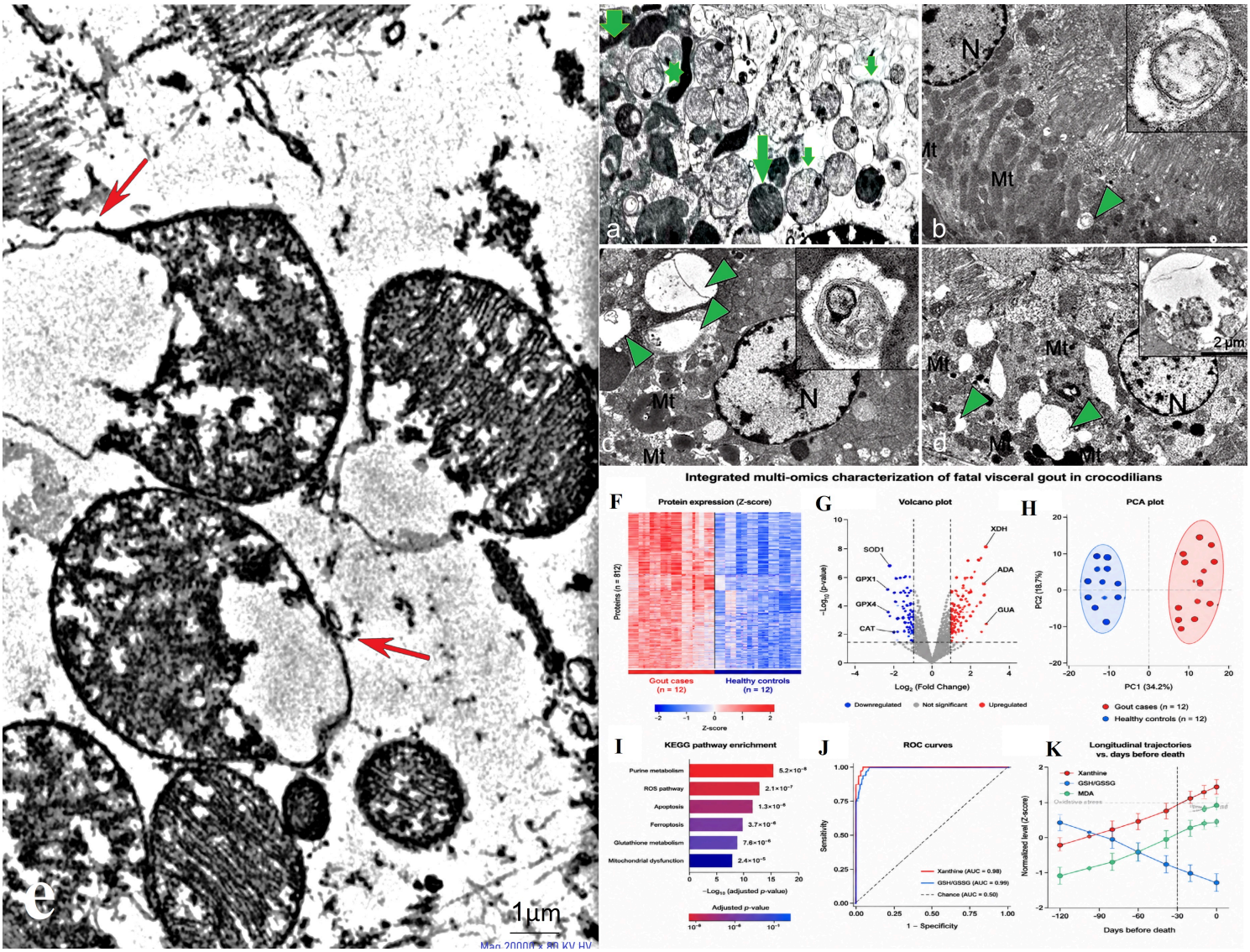


Figure 3

Ultrastructural and multi-omics characterization of fatal visceral gout in crocodilians. (A) Transmission electron microscopy, 28,000×: complete mitochondrial disintegration with rupture of outer and inner membranes and pathological calcium accumulation (case G5, Crocodylus palustris). (B) TEM, 20,000×: early-stage mitochondrial injury with swollen, dark, and fragmented mitochondria (case G4, Crocodylus suchus). (C) TEM, 20,000×: advanced-stage mitochondrial injury with extensive cytoplasmic vacuolation and progressive mitochondrial disintegration (case G4, C. suchus). (D) TEM, 20,000×: late-stage necroptotic cell death with autophagosomes containing degenerated mitochondria (case G4, C. suchus; inset: higher magnification, 500 nm). (E) TEM, 500 nm: mitochondrial degeneration in renal tubular epithelial cells with swollen mitochondria, marked cristolysis, electron-dense amorphous deposits, and eccentric membrane breakpoints (arrows) (case G1, C. palustris). (F) Heatmap of 347 differentially expressed renal cortical proteins demonstrating clear clustering of gout cases and healthy controls. (G) Volcano plot showing significantly altered proteins including upregulation of purine metabolism enzymes (XDH, ADA, GUA) and downregulation of antioxidant defenses (SOD1, GPX1, GPX4, CAT). (H) Principal component analysis of RNA-seq data showing clear separation between cases and controls (PC1 = 68% variance). (I) KEGG pathway enrichment analysis highlighting significant involvement of purine metabolism and reactive oxygen species pathways. (J) Receiver operating characteristic curves demonstrating excellent diagnostic performance of serum xanthine and GSH/GSSG ratio. (K) Longitudinal serum

metabolomics profiles showing progressive metabolic changes prior to death: early elevation of xanthine, progressive decline of GSH/GSSG ratio, and increasing malondialdehyde (MDA) concentrations. Scale bars: 500 nm (A, E), 1 μm (B–D). Stains: uranyl acetate and lead citrate (A–E). Abbreviations: TEM = transmission electron microscopy; XDH = xanthine dehydrogenase; ADA = adenosine deaminase; GUA = guanase; SOD1 = superoxide dismutase 1; GPX1 = glutathione peroxidase 1; GPX4 = glutathione peroxidase 4; CAT = catalase; GSH/GSSG = reduced glutathione to oxidized glutathione disulfide ratio; MDA = malondialdehyde; PC1 = principal component 1; AUC = area under the curve.

Supplementary Files

This is a list of supplementary files associated with this preprint. Click to download.

- SUPPLEMENTARYMATERIAL.docx